# Deciphering the diagenetic history of the El Abra Formation of eastern Mexico using reordered clumped isotope temperatures and U-Pb dating

Michael Lawson[1,†], Brock J. Shenton[1] , Daniel A. Stolper[2] , John M. Eiler[3] , E. Troy Rasbury[4] , Thomas P. Becker[1] , Charity M. Phillips-Lander[1,§], Antonio S. Buono[1] , Stephen P. Becker[1] , Robert Pottorf[1] , Gary G. Gray[1] , Don Yurewicz[1] , and Jonas Gournay[1]

[1] ExxonMobil Upstream Research Company, Spring, Texas 77389, USA [2] Department of Earth and Planetary Science, University of California, Berkeley, California, 94720, USA [3] Division of Geological and Planetary Sciences, California Institute of Technology, Pasadena, California 91125, USA [4] Department of Earth Sciences, Stony Brook University, Stony Brook, New York 11794, USA

† michael.lawson@exxonmobil.com

[§] Present address: Department of Geoscience, University of Nevada Las Vegas, Las Vegas, Nevada 89154, USA

Abstract

Carbonates form ubiquitously throughout the history of deposition, burial, and uplift of basins. As such, they potentially record the environmental conditions at the time of formation. Carbonate clumped isotopes provide the temperature of precipitation but can be internally reordered if the host rock is exposed to elevated temperatures over geologic time scales. Here, we exploited this kinetic behavior by analyzing multiple generations of cements that capture the range of environments experienced by the El Abra Formation from eastern Mexico. From this, we developed a quantitative diagenetic history for these different phases of cementation. We observed a 70 °C range in clumped isotope temperatures from 64 °C to 134 °C for these cements, which is not compatible with their inferred precipitation environments. This suggests that bond reordering occurred during burial but did not fully reorder all cements to a common apparent temperature. We reconstructed original cement growth temperatures and the isotopic signature of the parent fluids to show that precipitation from a marine pore fluid began at 125 Ma, contemporaneous with deposition, and continued throughout burial to temperatures of at least 138 °C at 42 Ma. We show that precipitation of equant cements, which occluded 90% of the pore space, was coincident with Laramide-related burial to depths greater than 3800 m. A U-Pb age of diagenetic calcite of 77.1 ± 3.6 Ma provides independent support for our estimates of the absolute timing of precipitation of two distinct phases of the paragenesis. This is the first demonstration of the utility of integrating U-Pb age dating with reordered clumped isotope temperatures to provide quantitative constraints on the time-temperature history of cementation. Such information may ultimately lead to advances in our understanding of the formational environments and geological processes

that drive diagenesis in carbonates for temperatures below the clumped isotope “blocking temperature.”

## INTRODUCTION

The impact of burial diagenesis on sedimentary carbonates remains enigmatic and difficult to predict. It can drive both dissolution and porosity development or cementation and porosity occlusion due to changes in the flux and chemistry of pore fluids and the ways in which these fluids react with the carbonate host rock (Choquette and Pray, 1970). Cements that form from these fluids can have a diverse range of morphologies and fabrics. Traditional approaches to constrain the origin of these cements suffer from significant limitations or yield underconstrained solutions. For example, petrographic and textural analysis of cements can be used to constrain the relative timing of important processes such as cementation, dissolution, and dolomitization. However, despite decades of research, it remains difficult to unambiguously link a given carbonate cement fabric to its depth and environment of precipitation or the specific geological events or processes that govern their occurrence. Furthermore, the qualitative nature of these constraints is difficult to place into broader geological studies that incorporate the timing of deposition, subsidence and burial, hydrothermal activity, and uplift. Such geological studies require temperature and absolute age constraints for carbonate precipitation, in addition to an understanding of the thermal history experienced by the formation. This information is critical for determining the diagenetic history of cement growth and thus the evolution and distribution of the fundamental rock properties required for many of the economic and societal uses of carbonate rocks.

The clumped isotope geothermometer, unlike traditional isotope thermometers such as $\delta^{18}O$-based thermometry (Epstein et al., 1953), provides carbonate precipitation temperatures independent of the $\delta^{18}O$ value of the fluid from which it precipitated (Ghosh et al., 2006; Eiler, 2007). With this precipitation temperature and the $\delta^{18}O$ value of the carbonate, one can then constrain the $\delta^{18}O$ value of the source fluid (McCrea, 1950). This technique has been used successfully to determine the temperature of carbonate precipitation associated with processes such as dolomitization (Ferry et al., 2011), hydrothermal fluid flow (Bristow et al., 2011), and burial diagenesis (Huntington et al., 2011; Budd et al., 2013; Dale et al., 2014; Ritter et al., 2015). An important aspect of the carbonate clumped isotope thermometer is that it is a homogeneous phase geothermometer. As such, any process that can “reorder” the isotopes amongst the isotopologues will alter the measured precipitation temperature. An example of such isotopic reordering in carbonates is represented by the following isotope exchange reaction:

$$Ca^{12}C^{16}O_3 + Ca^{13}C^{16}O_2{}^{18}O \leftrightarrow Ca^{12}C^{16}O_2{}^{18}O + Ca^{13}C^{16}O_3. \quad (1)$$

Recent studies of both natural and experimental samples have indicated that when calcite that is formed at near-surface temperatures (~25 °C) is exposed to temperatures in excess of 75–100 °C over geological time scales, the measured clumped isotope temperatures no longer reflect their original precipitation temperatures. Instead, they evolve and partially or totally reflect the exposure to these higher temperatures (Ghosh et al., 2006; Dennis and Schrag, 2010; Passey and Henkes, 2012; Shenton et al., 2015; Stolper and Eiler, 2015; Winkelstern and Lohmann, 2016). This occurs in the absence of recrystallization or open-system exchange with pore fluids. Recent studies have developed and applied experimentally calibrated kinetic models to quantify the extent of this reordering on carbonate phases with known precipitation temperatures in systems with well-constrained thermal histories (Henkes et al., 2014; Shenton et al., 2015; Stolper and Eiler, 2015; Lloyd et al., 2017).

In this study, we used clumped isotope–based thermometry of carbonates in combination with models of reordering (i.e., solid-state reorganization of rare isotopes in the carbonate lattice) to determine the original precipitation temperature of four generations of cements within the Hauterivian–Cenomanian El Abra Formation, which comprises the reef facies of the Valles–San Luis Potosi platform that is exposed in the Sierra de El Abra of northeastern Mexico (Fig. 1). The El Abra Formation was selected for this study because it has experienced significant and distinct phases of cementation as a result of burial diagenesis. These events have had a deleterious impact on the rock properties of what could have been a important reservoir for hydrocarbon accumulations in this region. We combined these measurements with a petrographically determined paragenesis and an independently constrained thermal history of the El Abra Formation, in conjunction with radiometric age constraints on carbonate precipitation. These various lines of evidence and arguments were then integrated to constrain the temperature and timing of precipitation of carbonate phases and the isotopic signature, and therefore origin, of the parent fluid from which they precipitated. This is the first attempt to couple clumped isotope measurements with a well-characterized paragenetic history in order to constrain the time and temperature of cement growth in deeply buried sedimentary basins when the original temperature and timing of precipitation are unknown.

## GEOLOGIC SETTING

The Lower Cretaceous Valles–San Luis Potosi initially developed as an isolated rudist platform with a steep eastern windward margin. Periodic subaerial exposure significantly influenced the development of porosity and permeability of the reef facies (Minero, 1991). To the east of the Valles–San Luis Potosi, finer-grained slope facies were deposited between it and the isolated Tuxpan (or “Golden Lane”) platform located on the Tamaulipas arch along the eastern Tampico-Misantla Basin. The Tampico-Misantla Basin lies

between these two features. The El Abra Formation represents the reef margin of the Valles–San Luis Potosi carbonate platform.

Subduction of the Farallon plate (or equivalents) during the Late Cretaceous and early Cenozoic deformed the continental interior of Mexico during the Hidalgoan orogeny, creating the Sierra Madre Oriental, a basement-detached thrust belt that propagated from west to east (Guzman and De Cserna, 1963; Gray and Lawton, 2011). Subsidence associated with the eastward-advancing Late Cretaceous–early Cenozoic tectonic load ultimately drowned the Sierra de El Abra platform interior in the Coniacian–Santonian. Clastic sediment shed from emerging thrust sheets fouled carbonate production and continued to fill the basin during the early Cenozoic (Guzman and De Cserna, 1963; Gray et al., 2001). The Valles–San Luis Potosi platform was likely buried during deposition of the Maastrichtian–Campanian Mendez Formation (Aguillón et al., 1999). The coeval appearance of clastic sediment and increasing accommodation during the Late Cretaceous to early Cenozoic are attributed to Hidalgoan (following Guzman and De Cserna, 1963; Gray and Lawton, 2011) basement-detached contractional deformation, which formed the Sierra Madre Oriental fold belt.

Thrust sheets associated with the Sierra Madre Oriental form a series of linear topographic ridges west of the study area and are likely rooted in a weak Albian evaporite and Jurassic detachment (Fig. 1). The Sierra de El Abra stands as a prominent ridge east of the leading edge of the Sierra Madre Oriental thrust belt, and a thrust fault is mapped along its eastern base of slope (Aguillón et al., 1999). Longer-wavelength folds east of the leading edge of the Sierra Madre Oriental thrust belt are possibly inverted normal faults, and we suggest that these basement-involved structures were responsible for a small degree of exhumation (Fig. 1). It is worth noting that the Sierra de El Abra region was located on the platform margin, and there remains uncertainty as to whether the ~500 m of structural relief between the El Abra Formation at Sierra de El Abra and the El Abra-1 well presented in Figure 1 was created by contractional deformation along a reverse fault, or if it represents original bathymetric relief along the platform margin during Cretaceous deposition (Gray et al., 2001). If the Sierra de El Abra is a detached thrust sheet that was tectonically exhumed (e.g., Wolfe, 2012), the El Abra Formation may have cooled during the Eocene eastward advance of the thrust system. In addition to cooling, the tectonic deformation may have promoted additional fracturing, pressure solution (and reprecipitation), and fluid flow from pressure or topographic gradients during the Cenozoic within the Valles–San Luis Potosi platform region. On the basis of fluid inclusion microthermometry reported by Gray et al. (2001), the El Abra Formation was buried to temperatures of at least ~165 °C. This implies significant postorogenic (Eocene to Oligocene) burial.

Following contractional deformation in the late Paleocene–early Eocene, apparently rapid exhumation of the Sierra Madre Oriental thrust belt and adjacent foreland basin occurred from ca. 35 Ma to present. Most of the

evidence for this comes from modeling of apatite fission-track (AFT) lengths and ages (Gray et al., 2001), along with compilations of offshore isopach maps (Galloway et al., 2000) and depositional rates (Yarbuh and Contreras, 2017) that suggest rapid denudation of the onshore region. The geologic map (Aguillón et al., 1999) also hints at a basinwide reorganization, as post-Eocene sediments are limited to areas near the coastal plain, with much of the area to the west stripped to Cretaceous-age strata (Fig. 1).

The samples analyzed in this study were taken from the El Abra Formation, which is exposed in quarries of the Sierra de El Abra. The Sierra de El Abra may have hosted over 1 billion barrels of oil prior to exhumation (Pottorf et al., 1996). However, burial diagenesis drove significant pore-occluding cementation that significantly deteriorated reservoir quality within the El Abra Formation (Suter, 1984; Minero, 1988, 1991; Gray et al., 2001). This system was selected for study because it has a well-constrained thermal history and a well-characterized paragenesis of major cementation events that dictated the reservoir quality and potential hydrocarbon storage capacity of the El Abra Formation (Minero, 1991).

We employed a paragenetic model for the relative timing of growth of four generations of carbonate cements within the El Abra Formation (Minero, 1988). Three generations of these cements developed during the burial phase of the basin history and dominate the pore space in the El Abra Formation. Initial porosity loss is thought to be the result of early marine cementation. This is preserved as two generations of radiaxial calcite: The first phase is a fibrous radiaxial calcite that lines pore space (R1), followed by a secondary, coarse radiaxial cement (R2). Previous studies suggested that these fabrics precipitated in a shallow (<1 km) marine environment in open exchange with Cretaceous seawater, based on the $\delta^{18}O$ of the cement (Minero, 1988). Radiaxial cementation was followed by precipitation of blocky, equant cement (E1) that occupies up to 90% of the pore space. This cement is thought to have precipitated from meteoric fluids in an open, shallow environment at temperatures near 25 °C prior to rapid Laramide-related burial (Minero, 1988). Finally, a fourth generation of cement, also equant in fabric, formed during the uplift phase of the basin history (E2). This cement precipitated in vugs that were formed from anhydrite dissolution following early Paleogene deformation and invasion of meteoric waters during exhumation (Minero, 1991).

## METHODS

### Sample Collection

Rock samples analyzed in this study were characterized and discussed in Gray et al. (2001). Samples were all obtained from the same stratigraphic interval (El Abra Formation) that crops out in three locations in the Cuidad Valles region of Mexico. Sample names relate to their location within this region as follows: CAN samples were obtained from Cementos Anahuac, CMEX samples were obtained from Cementos Mexicanos, and TAN samples

were obtained from the Taninul Quarry. The location of the study site is provided in Figure 1, and the thermal history for the El Abra Formation at a central point between sample locations is provided in Figure 2. The close proximity (<10 km) of these different sample locations ensures that the El Abra Formation likely experienced essentially the same thermal history at each location. However, each cement phase will have experienced slightly different thermal histories. The relative timing of the different cement phases dictates the extent to which each phase was exposed to this thermal history post-precipitation. In this context, the fibrous radiaxial cement (phase 1) experienced more of the thermal history than the equant cement (phase 3), given their relative positions within the paragenesis. This is described in more detail later herein.

## Petrographic Analysis

Lining and coarse radiaxial and equant cements were identified in thin sections using the previous petrographic framework given in Minero (1988). Cement phases were selected for isotopic analysis following initial petrographic characterization to identify any potential recrystallization, because recrystallization can overprint primary isotopic signatures. As such, samples were selected that displayed little or no evidence of recrystallization or other forms of alteration (for examples of samples CMEX6 and CMEX3, see Figs. 3 and 4). Thin sections of carbonate components were characterized using optical and cathodoluminescence (CL) microscopy with a Reliotron III cathodoluminescence instrument from Relion Industries at ExxonMobil Upstream Research Company. The luminoscope was operated between 200 and 300 mA and 10 and 15 kV, and images were taken with a Coolsnap-Procf digital camera with exposure times ranging from 20 to 30 s. Based on the petrographic observations, ~10 mg aliquots of carbonate powders were milled with 0.5 mm or 1 mm dental burs and homogenized for isotopic analyses.

## Carbon and Oxygen Isotope Analyses

Isotopic analyses ($\delta^{13}C$, $\delta^{18}O$, and $\Delta_{47}$) on the carbonate cement phases were performed in June 2013 at the California Institute of Technology on a custom-made automatic vacuum line attached directly to a Thermo MAT 253 mass spectrometer (Passey et al., 2010). Most measurements were replicated twice, while three samples were only analyzed once (CMEX-3, CMEX-6, and TAN-101) due to limited sample quantities. When carbonates are subjected to phosphoric acid digestion, these clumped isotopologues are released as multiply substituted forms of $CO_2$, including the mass 47 amu isotopologues $^{13}C^{16}O^{18}O$, $^{12}C^{17}O^{18}O$, and $^{13}C^{17}O_2$. The $\Delta_{47}$ value reports the excess of these isotopologues relative to $CO_2$ having the same bulk isotopic composition ($\delta^{13}C$, $\delta^{18}O$, and $\delta^{17}O$ value) and a random isotopic distribution of isotopes among all isotopologues. At isotopic equilibrium, the $\Delta_{47}$ value (i.e., clumped isotope excess) is solely a function of temperature and independent of the $\delta^{18}O$ and $\delta^{13}C$ values of the carbonate (Ghosh et al., 2006; Schauble et al.,

2006). The $\delta^{13}C$ and $\delta^{18}O$ values of $CO_2$ were measured by comparison of samples to a gas with a known isotopic composition using an ion correction algorithm in the Isodat software program and standardized to the Vienna Peedee belemnite (VPDB) scale for carbon and oxygen isotope measurements (Huntington et al., 2009). Carbonate $\delta^{18}O$ values were calculated from the $CO_2$ values assuming that the isotopic fractionation factor between calcium carbonate and $CO_2$ for phosphoric acid digestion at 90 °C is 1.00821 (Swart et al., 1991). The $\Delta_{47}$ values were standardized by comparison of samples with gases that were heated to 1000 °C and reported in the Ghosh et al. (2006) reference frame. Clumped isotope values are also reported in the absolute reference frame. However, low-temperature equilibrated gases (25 °C) were not routinely measured at the time of analysis. Consequently, these values were calculated using the secondary transform (Dennis et al., 2011) and therefore should be considered approximate. Standard reproducibility of a Carrara marble was 2.111‰ ± 0.057‰, –2.024‰ ± 0.028‰, and 0.369‰ ± 0.019‰ for measured $\delta^{18}O$, $\delta^{13}C$, and $\Delta_{47}$ values, respectively, based on one standard deviation error, as compared to the long-term $\Delta_{47}$ average for this standard of 0.352‰ (in the Ghosh et al. [2006] or “Caltech” intralaboratory reference frame). The $\Delta_{47}$ values were converted to temperatures using the calibration presented by Stolper and Eiler (2015).

## U-Pb Isotope Analysis

U-Pb laser-ablation (LA) analyses were made using a New Wave U213 laser coupled to an Agilent 7500cx quadrupole inductively coupled plasma–mass spectrometer (ICP-MS) at the Facility for Isotope Research and Student Training at Stony Brook University on sample CMEX-3. Element maps demonstrated that the host rock and cement phases are distinct, supporting other petrographic evidence that these samples exhibit little evidence for fluid-rock interaction (see Fig. DR1 of this map in the GSA Data Repository[1]). Element maps were used to select areas for U/Pb LA-ICP-MS analysis by identifying cement phases with high U/Pb concentration ratios and low $^{207}Pb/^{206}Pb$ ratios. A natural carbonate standard from the Permian Reef Complex (Walnut Canyon standard) with high U/Pb and fairly homogeneous distribution of U and Pb concentrations and Pb isotope composition was used in this study (Parrish et al., 2013). The highest U/Pb and lowest $^{207}Pb/^{206}Pb$ values, which are most favorable for providing precise ages, were found in small veins that crosscut the radiaxial cements and terminated in the equant cement (see Figs. DR2–DR4 [see footnote 1]). As such, these cements must postdate radiaxial cementation but predate precipitation of the equant cements (see the Appendix for a more detailed description). Data were reduced in Iolite to correct for baseline, drift, and downhole fractionation (Paton et al., 2011). The reduced data were evaluated in IsoExcel (Ludwig, 2012).

## THERMAL HISTORY MODELING

Paleothermometry techniques, coupled with basin modeling, provide a means of constraining aspects of the thermal history of the El Abra Formation. We developed a one-dimensional (1-D) basin model for the Sierra de El Abra location where the samples were obtained to simulate the burial history using regional formation isopachs as a means of constraining the overburden thickness and lithology. This burial history was used as a basis for developing a thermal history for the El Abra Formation at this location. Because the El Abra Formation is presently exposed at the surface at Sierra de El Abra due to erosion of since-removed overburden, the stratigraphy preserved within the adjacent, downdip Misantla Basin was used to help constrain the burial history at the location where the samples were taken in the Sierra de El Abra. In this case, the Abra-1 well (located 50 km north of the sample locations) penetrated the El Abra Formation and was used to help constrain the thickness of a small portion of the now-missing overburden. In addition, regional isopach data from wells and published geologic maps (e.g., Aguillón et al., 1999) from the Tampico-Misantla Basin were used to estimate Paleogene thicknesses in particular.

A proprietary ExxonMobil basin modeling software package, Stellar, was used to develop the thermal history of the El Abra Formation. The Stellar software includes a lithology-dependent decompaction-compaction algorithm, which can be used as a basis for estimating changes in density and porosity that ultimately feed into variations in thermal conductivity through time (e.g., Shenton et al., 2015). The thermal history for this region was realized using (1) an estimate of basal heat flow through time, (2) sediment compaction state and lithology-dependent thermal conductivities, (3) lithology-dependent radiogenic heat production, and (4) surface temperature estimates, which range from submarine to elevation-dependent. As a first approximation, a constant heat flow of 55 $mW/m^2$ was used to develop a base case model, as downhole vitrinite profiles and heat-flow measurements were not available to independently calibrate the model. An additional scenario was developed with a higher background heat flow of 65 $mW/m^2$ to explore any sensitivities associated with the uncertainty of heat flow through time in the thermal history of the El Abra Formation at this location. Sediment compaction was assumed to be under normal hydrostatic conditions, and the thermal conductivity and concentration of radiogenic heat production per meter varied accordingly. Surface temperatures were estimated using surface temperature and latitude relationships (e.g., Wygrala, 1989; Frakes et al., 1992) coupled to a proprietary plate model that tracks surface location through time.

We lack the ability to know the precise thickness and lithologies of eroded overburden, but there are several paleothermometric proxies that can be used to constrain the resulting thermal history derived from the burial history. This, in turn, helps to validate the burial history, assuming that the thermal history can be accurately transformed into depth. Without geologic context, there are many nonunique solutions to this problem, but local

geologic constraints and multiple paleothermometric proxies often greatly reduce the degrees of freedom.

The prograde burial (and thermal) history was constrained using illite age analysis (IAA), which dates the diagenetic transformation of smectite to illite (Pevear, 1999), typically occurring between 70 °C and 90 °C. The model was calibrated by comparing IAA results from the Lower Cretaceous Upper Tamaulipas Formation at Sierra de El Abra (see Gray et al., 2001) with hypothetical transformation ages using the kinetic model of Huang et al. (1993) at 50 ppm K concentration. Optical fluid inclusion microthermometry of samples obtained from the El Abra Formation in quarries at Sierra de El Abra yielded a homogenization temperature of ~165 °C, which provided a minimum for the maximum burial temperature of the El Abra Formation (Gray et al., 2001). The apatite fission-track data used to constrain the retrograde thermal history presented in Gray et al. (2001) were updated by remodeling apatite fission-track lengths and ages using a track length annealing model (Ketcham, 2005) implemented in HeFTy (Ketcham et al., 2007) that indicates rapid exhumation at ca. 33 Ma. The integrated thermal history presented here suggests that the onset of rapid burial was coincident with the Laramide orogeny at ca. 65 Ma, maximum burial was achieved in the Oligocene, and exhumation began ca. 33 Ma and accelerated through the Miocene (Fig. 2). The base case thermal history we use in the clumped isotope model presented later herein honors the maximum burial temperature constraints provided by fluid inclusion microthermometry. In contrast, the high-heat-flow scenario gives rise to a maximum burial temperature of 193 °C at the same time (Fig. 2). In general, the base case burial history and resulting thermal history follow that of Gray et al. (2001) at this location, except that a subtle Paleocene tectonic exhumation (and cooling) was also included in the scenario.

## RESULTS AND DISCUSSION

Petrographically, the R1 cement exhibits a distinct boundary with the later E1 cement in both plain light and under CL (Figs. 3 and 4). The R2 cement sampled from CMEX 6 also displays a distinct boundary with the R1 cement. However, the R2 cement displays a less distinct boundary with the E1 cement. It is therefore possible that the outer portions of the R2 cement may have experienced some partial recrystallization. As such, we targeted the center of the R2 cement to minimize any contribution of potentially altered R2 cements in the sample. The equant cements were nonluminescent in all samples. However, both generations of radiaxial cements exhibited patchy luminescence in samples CMEX 3 and CMEX 6 (see Figs. 3 and 4). It remains ambiguous as to whether luminescence in radiaxial cements reflects alteration or not. Radiaxial cements are thought to precipitate dominantly from marine pore fluids (Kim and Lee, 2003). In such environments, temporal and spatial changes in the redox state of the pore fluids are possible and could give rise to bands of cements that display different luminescence under CL even in the absence of recrystallization. The recent study of Ritter

et al. (2015), who compared multiple geochemical proxies (including clumped isotope analysis) with luminescence, also demonstrated that luminescence of these fabrics does not *a priori* require a recrystallization overprint, and that these fabrics can still be targeted to yield insights on primary marine fluid signatures. Nonetheless, we tried to target the least luminescent regions of the cements to minimize any potential risk of sampling a diagenetically altered part of the cement. While it is possible that the R1 and R2 samples contained minor amounts of recrystallized cement, for reasons we will expand on later herein, we believe that these samples most likely reflect primary unaltered fabrics.

The average $\delta^{13}C_{VPDB}$ and $\delta^{18}O_{VPDB}$ values of the different carbonate cement generations display significant variability (see Table 1) and show strong covariance ($R^2 = 0.84$). Individual measurements of $\delta^{13}C$, $\delta^{18}O$, and $\Delta_{47}$ for heated gases, standards, and samples are provided in the Data Repository in Table DR2 (see footnote 1). These data are plotted in Figure 5 alongside previous measurements made on these generations of cements (Woo, 1986; Brennan, 1994). The earliest paragenetic phase in this study, the fibrous radiaxial calcite (R1), has $\delta^{13}C_{VPDB}$ (+2.5‰) and $\delta^{18}O_{VPDB}$ values (–2‰ to –2.5‰) similar to previously measured nonluminescent bivalves and radiaxial fibrous calcite from the studied unit (Woo et al., 1993). These values are consistent with precipitation at 20 °C from mid-Cretaceous surface seawater with $\delta^{18}O_{VSMOW}$ of –1.2‰ (Kim and O'Neil, 1997), in agreement with a dominantly ice-free global hydrosphere at this time (Shackleton and Kennett, 1975). Thus, the isotopic composition of the R1 calcite supports the inferences from petrographic studies, i.e., that it precipitated in a shallow burial setting from marine-derived pore fluids. The R2 cement is isotopically distinct from the earlier R1 calcite, with $\delta^{13}C_{VPDB}$ of +1.6‰ and $\delta^{18}O_{VPDB}$ of –5.2‰. The third phase within the paragenesis, the E1 cement, has ranges in $\delta^{13}C_{VPDB}$ and $\delta^{18}O_{VPDB}$ that vary from values similar to that of the R2 cement to even lower values ($\delta^{13}C_{VPDB}$ = 0.8‰ to 1.7‰ and $\delta^{18}O_{VPDB}$= –5.2‰ to –7.9‰). The fourth generation of cement, the uplift-related, equant, vug-filling cement (E2), is characterized by the lowest C and O isotope ratios of any of the cement phases ($\delta^{13}C_{VPDB}$ = 0.4‰ to 0.9‰, $\delta^{18}O_{VPDB}$ = –11.8‰ to –12.9‰).

The carbonate $\Delta_{47}$ values for the different generations of cements range from 0.528‰ ± 0.011‰ for an R1 cement (CMEX3) to 0.413‰ ± 0.002‰ for an E1 cement (TAN104). These clumped isotope signatures correspond to a 70 °C range in apparent temperatures for the different phases within the paragenesis (Table 2). These temperatures display a systematic relationship to texture but no straightforward correlation with $\delta^{13}C_{VPDB}$ and $\delta^{18}O_{VPDB}$ values (see Figs. DR5 and DR6 [see footnote 1]). Specifically, the R1 cements from two samples (CMEX 3 and CMEX 6) yielded temperatures of 64 ± 8 °C ($n$ = 1) and 64 ± 9 °C ($n$ = 1), respectively, the R2 cement yielded a temperature of 81 ± 10 °C ($n$ = 2), the E1 cements varied between 97 ± 11 °C ($n$ = 2) and 134 ± 17 °C ($n$ = 2), and the E2 cements from two samples (TAN 101

and CAN 11A) yielded temperatures of 68 ± 9 °C ($n$ = 2) to 74 ± 9 °C ($n$ = 1). Analysis of the host limestone yielded an apparent temperature of 83 ± 10 °C ($n$ = 2). The temperatures measured for the burial-related cements (R1, R2, and E1) exceed the expected precipitation temperatures based on their inferred shallow environment of growth (Minero, 1988). Such elevated temperatures are consistent instead with either recrystallization in the subsurface or isotopic reordering by solid-state lattice-scale atomic mobility.

## Clumped Isotope Reordering in the Zone of Partial Retention

We hypothesize that the various burial-related carbonate cements (R1, R2, and E1) present in these rocks precipitated at temperatures lower than their measured apparent temperatures and then experienced partial reequilibration through solid-state isotopic reordering during further burial. This process elevated the apparent temperatures of all cements and reduced the differences in apparent temperatures between different fabrics. However, because the process occurred at temperatures below the nominal "blocking temperature" for clumped isotope reordering, apparent temperatures of different cements did not fully equilibrate with each other, and none fully equilibrated to the environmental temperature.

We further developed this hypothesis using the paired "reaction-diffusion" model of Stolper and Eiler (2015), which quantifies the impact of reordering on the clumped isotope apparent temperature, given some specified initial precipitation temperature and a subsequent temperature-time history. We recognize here that other models have been proposed that quantify the impact of heating and subsequent cooling on C-O bond reordering in carbonate minerals, notably the studies of Passey and Henkes (2012) and Henkes et al. (2014). These studies also suggest that different cement phases may exhibit contrasting propensities to solid-state reordering, potentially based on differences in trace-element composition or defect structures of the mineral lattice. It is possible that the application of these different models may give rise to different predictions of the extent of reordering. However, a comparison of these different kinetic models on the extent of clumped isotope reordering is beyond the scope of this study. Further, we know of no external constraints on the Arrhenius parameters for these specific cements. We therefore make the assumption here that each distinct cement phase within the paragenesis exhibits the same kinetic properties for reordering in response to heating and cooling.

We implemented the model of Stolper and Eiler (2015) using the thermal history independently developed for the El Abra Formation (Fig. 2; Appendix) to solve for the initial growth temperature of each cement that would result in the observed apparent temperature after partial reequilibration during subsequent burial (presented in Table 3). At a given point on the thermal history, one assumes that a cement is precipitated at the temperature defined by the thermal history. The cement is then exposed to the reordering model based on the remainder of the thermal history post-precipitation. The

blue to red lines in Figure 6 represent increments of 5 °C in the original cement growth temperatures that are subsequently reordered as a result of the remainder of the thermal history (moving from right to left in Fig. 6). These result in modified apparent temperatures that would be measured present day. For example, an original cement growth temperature of 25 °C would give rise to a present-day apparent temperature of ~68 °C. This ultimately creates a transfer function that allows us to take any final reordered clumped isotope temperature (i.e., that which we measured) and link it back to the original precipitation temperature for any arbitrary time step on the thermal history. Having reconstructed the original precipitation temperatures (based on the reordering model) of the different cement phases, we can then refer back to our independently known thermal history to establish the timing of precipitation of each phase of cementation (Fig. 7). We propagated our analytical uncertainty for clumped isotope signatures through the model to derive uncertainties in the restored original precipitation temperatures and, from this, an uncertainty in the timing of precipitation (Table 3). With the exception of the vug-filling cements, we assumed that samples formed during burial and not uplift and experienced no diagenesis after formation.

Our model predicts that the two phases of radiaxial cements formed at temperatures of ~15 ± 13 °C (R1 cements) and 43 ± 15 °C (R2 cement), respectively. These restored temperatures of cement growth suggest that the R1 cement precipitated contemporaneous with sediment deposition at ca. 125 Ma, with a minimum permissible age of 89 Ma. These temperatures and ages correspond to a range in the depths of precipitation of between the seafloor and 100 m. Similarly, the R2 cement precipitated at ca. 80 Ma, with a range from 53 to 93 Ma. This corresponds to a depth of 320 m, with a range in the depth of precipitation from 80 to 1000 m (Fig. 7). U-Pb dating of a cemented vein that crosscuts through the radiaxial cements in the CMEX 3 sample provides an age of 77.1 ± 3.6 Ma, in good and independent agreement with our modeled ages from the restored clumped isotope temperatures for the two generations of radiaxial cements. As described previously, this vein is required to have precipitated after the radiaxial fabrics and before the equant cements in which it terminates. In contrast, the dominant pore-occluding E1 cements are required to have formed over a period of up to 17 m.y. This phase of cementation began at ca. 52 ± 2Ma at a temperature of 70 ± 20 °C. This corresponds to a depth of ~1200 m, with a range from 950 to 1400 m. Precipitation of this cement continued during burial to temperatures of ~138 °C, and within a range of 108 to 138 °C, at depths in excess of 3800 m prior to maximum burial between 46 and 33 Ma. We note here that there is a small overlap in the temperatures of the different phases given the propagation of analytical uncertainty through the reordering model. However, the results are consistent with the inferred paragenesis and the U-Pb age from the crosscutting cement. As such, we believe they provide robust quantitative constraints on the time-temperature

history of cementation in the El Abra Formation. These temperatures and depths conflict with the inferred environment of growth for these E1 cements, which was previously inferred to be in a shallow environment at temperatures near 25 °C (Minero, 1988). Instead, the precipitation of the E1 cements appears to be related to rapid Laramide-related burial and may have coincided with the first oil charge to these reservoirs, which is suggested to have migrated into the El Abra Formation during the Paleogene (Gray et al., 2001). Finally, we consider the temperatures associated with the exhumation-related E2 cements to reflect primary precipitation temperatures, as they have previously been shown to have formed after peak burial temperatures during cooling and uplift (Minero, 1991). As such, they did not experience burial temperatures above their measured growth temperatures. Our thermal history modeling suggests that these cements formed at a depth of ~1000 m at 25 Ma.

An inherent assumption of our modeling work is that the thermal history we derived for the El Abra Formation is accurate. In reality, it is difficult to assess the uncertainty of any thermal history. However, in this case, we have numerous constraints beyond which we cannot deviate. For example, we know that the El Abra Formation must have experienced temperatures of at least 165 °C because of the consistency of optical fluid inclusion thermometry observations for this formation at the sampling locations and regionally. Similarly, the constraints provided by IAA and AFT place quantitative time-temperature constraints on the burial and exhumation of the El Abra Formation. It is possible that the El Abra Formation experienced temperatures hotter than 165 °C. We therefore assessed the impact of an elevated heat flow on the clumped isotope reordering, as described in the thermal history modeling section above. The thermal history in this scenario honors the constraints provided by IAA and AFT, but the basal heat flow used in the model was increased by 10 $mW/m^2$. In this scenario, the El Abra Formation reaches a maximum temperature of 193 °C as a result of the increased basal heat flow at 33 Ma. In addition to a higher maximum burial temperature, this elevated heat flow also results in an increase in the amount of time spent above 100 °C from 20 m.y. for the base case thermal history to 25 m.y. for the high-heat-flow scenario. We again applied the model of Stolper and Eiler (2015) to model the impact of this enhanced thermal history on the evolution in the clumped isotope signature of a hypothetical cement that formed at 25 °C at the time of deposition. This is analogous to the R1 cement in this study. In this scenario, the clumped isotope temperature of the cement experiences significant reordering, and we estimate it would record a clumped isotope temperature of 139 °C at present day (see Fig. DR7 [see footnote 1]). This temperature is hotter than any of the cements we measured in this study. This analysis of the sensitivity of clumped isotope reordering to the defined thermal history suggests that our base case thermal history applied to derive original precipitation

temperatures is reasonable, and that any error in the thermal history we apply to derive the temperature and time of precipitation is relatively small.

We also recognize there may be some uncertainty as to whether the isotopic signatures of the R1 or R2 cements reflect primary signatures, or if they were diagenetically altered during burial. The bulk isotopic signature of the R2 cement is very similar to that of the lower-temperature E1 cement, which could suggest that the R2 cement underwent partial or total recrystallization immediately prior to the precipitation of the equant cement. In this scenario, the isotopic signature of the R2 phase would now reflect the pore-fluid chemistry at the time of alteration. However, this would require that this recrystallization has maintained the radiaxial fabric while precipitating a totally different cement fabric from the same pore fluid during growth of the equant cement. Further, each phase of the paragenesis exhibits distinct clumped isotope temperatures. This suggests that if recrystallization has impacted the primary signatures, it has done so in a way that maintained distinct compositions for each of the phases. Alternatively, it is possible that the distinct temperatures for each phase of the paragenesis are not associated with recrystallization and instead reflect differences in the sensitivity of each cement phase to reordering as proposed by Passey and Henkes (2012). We consider this unlikely because the reconstructed ages of each cement phase that we estimate from our reordering model are consistent with the inferred environment of precipitation and, as discussed already, the independent age constraint provided by the U-Pb age dating of the crosscutting cement. We suggest that the most likely interpretation is that the different cements are original unaltered fabrics that exhibit broadly similar properties for bond reordering given the internal consistency of the interpretation provided by the petrographic, isotopic, and radiometric age dating analyses. If diagenetic alteration of the cements has occurred or differences in clumped isotope reordering properties do exist, these have had minimal, if any, impact on the different phases within the paragenesis and do not change the interpretation we provide here.

## Implications for Pore-Water Chemistry—Marine versus Meteoric

The restored precipitation temperatures presented here allow us to estimate the chemical conditions of cementation in the context of the El Abra Formation thermal history. Specifically, we utilized the restored precipitation temperatures and measured $\delta^{18}O_{VPDB}$ values to estimate the $\delta^{18}O_{VSMOW}$ value of the precipitating fluids using an equation for the temperature-dependent $\delta^{18}O$ difference between calcite and water (Kim and O'Neil, 1997). As with the estimates of the timing of precipitation discussed earlier herein, we propagated the uncertainty of the restored temperature to calculate the uncertainty in the restored $\delta^{18}O_{VSMOW}$ values. We present calculated $\delta^{18}O_{VSMOW}$value of the parent fluid based on both the measured apparent and restored precipitation temperatures (along with the $\delta^{18}O_{VPDB}$ values) in Figure 8. The $\delta^{18}O_{VSMOW}$ values of the parent fluid calculated using unrestored temperatures for burial-related R1, R2, and E1 cements are significantly

heavier (more positive) compared to restored values. The $\delta^{18}O_{VSMOW}$ values calculated from the unrestored clumped isotope temperatures range from 6.8‰ ± 1.5‰ to 10.8‰ ± 1.4‰ (Fig. 8). Importantly, these enriched isotopic signatures are typical of closed systems in which the $\delta^{18}O_{VSMOW}$ value of the fluid is elevated due to fluid-rock reactions at high temperatures. This contrasts with the previous interpretation that these cements formed at shallow depths from marine and early meteoric pore fluids.

Using the restored temperatures significantly shifts the estimated $\delta^{18}O_{VSMOW}$ values of the formational fluids (Fig. 8). The $\delta^{18}O_{VSMOW}$ of the parent fluid that precipitated the radiaxial cements changes from 6.8‰ ± 1.5‰ to 7.5‰ ± 1.4‰ for the uncorrected values to –2.2‰ ± 3.1‰ to +0.5‰ ± 2.8‰ for the temperature-corrected values. These restored $\delta^{18}O_{VSMOW}$ values are consistent with precipitation from Cretaceous seawater in tropical regions based on modeled $\delta^{18}O_{VSMOW}$ values (Zhou et al., 2008). In contrast, the $\delta^{18}O_{VSMOW}$ values for the parent fluids associated with the E1 cements shift from 9.1‰ ± 1.5‰ to 10.8‰ ± 1.9‰ for uncorrected temperatures to 5.2‰ ± 2.7‰ to 11.1‰ ± 2.8‰ for restored temperatures. The restored cement phases now display a positive relationship between the corrected original temperature and the $\delta^{18}O_{VSMOW}$ value of the precipitating fluid (Fig. 8). This evolution in the oxygen isotopic signature of fluids, from the radiaxial to the burial-related equant (E1) cement phases, for a narrow range in carbonate oxygen isotopic signatures, has implications for the evolution in the pore-fluid chemistry and cementation of the El Abra Formation. Specifically, the restored temperatures and corrected $\delta^{18}O_{VSMOW}$ values for the R1 and R2 cement parent fluid suggest that these cements precipitated in an open system from marine pore fluids in a water-buffered environment (consistent with previous inferences), but that E1 cements precipitated from an evolving marine pore fluid in a closed system at depth through fluid-rock interaction at increasingly elevated temperatures (Allan and Matthews, 1982). Our findings argue against the introduction of meteoric fluid during the precipitation of E1 cements, as inferred from prior petrographic and $\delta^{18}O$ interpretations of the mineral fabric (Minero, 1988). The shift to more negative $\delta^{18}O_{VSMOW}$ values for the parent fluid of the exhumation-related E2 cements (–0.9‰ ± 1.4‰ to –3.0‰ ± 1.4‰) presumably reflects a return to more open-system conditions and a change in pore-fluid chemistry. This parent fluid may have consisted of a mixture of primary marine-derived pore fluids and invading meteoric waters with light (more negative) $\delta^{18}O_{VSMOW}$ values that were introduced during exhumation. This is consistent with the inferred precipitation environment and fluid origin from petrographic analysis (Minero, 1991), and it provides further confidence in the reordering modeling and interpretations discussed earlier herein.

## CONCLUSIONS

The integration of carbonate clumped isotope analyses coupled with kinetic models of clumped isotope reordering and independent age constraints from U-Pb dating demonstrates that key porosity-destroying cement phases in the

El Abra Formation precipitated from a common marine pore fluid. Our revised thermal history suggests that the El Abra Formation was exposed to temperatures in excess of 70 °C for ~17 m.y. from ca. 50 Ma to 33 Ma, with ~5 m.y. spent above 150 °C. This thermal history appears to have been sufficient to partially reorder the clumped isotope compositions of the carbonates, elevating their apparent temperatures above their original precipitation temperatures, but not completely reordering them. The measured temperatures are incompatible with the inferred precipitation environments indicated by petrographic analyses. Correction for the thermal history using a kinetic model of clumped isotope reordering restores these carbonates to temperatures that are reasonable precipitation temperatures. Importantly, the restored temperatures and depths for burial-related E1 cement growth (1200–3800 m) provided by our kinetic modeling of carbonate clumped isotope data greatly exceed the previous qualitative predictions provided by petrographic analysis (<1000 m). Application of the restored temperatures to calculate parent fluid isotopic signatures also results in $\delta^{18}O_{VSMOW}$ values that are consistent with the revised environments of cement growth. These $\delta^{18}O_{VSMOW}$ values provide insights into the evolution of $\delta^{18}O$ values of the pore waters and the environments of carbonate precipitation. Specifically, we have shown that equant cementation that occluded 90% of the pore space of the El Abra Formation in the Sierra de El Abra precipitated from a marine pore fluid, and not a meteoric fluid as suggested by previous studies. Further, this cementation occurred during rapid burial at depths greater than previously suggested. This has direct implications for the prediction of important properties of the El Abra Formation, such as porosity, on a regional basis. This work shows that the carbonate clumped isotope geothermometer, in conjunction with laboratory-derived kinetics of isotopic reordering, can provide new constraints on thermal histories of burial diagenesis and cementation in the temperature interval over which measured clumped isotope temperatures begin to be reordered (>100 °C). Understanding the age-temperature and depth relationship for cement formation may provide new insights on the fluid compositions and geologic processes that drive cementation in sedimentary carbonates.

## APPENDIX

### U-Pb Dating

A slab of CMEX3 that had been sampled for clumped isotopes was tested for potential for U-Pb dating using LA-ICP-MS with an Agilent 7500cx coupled to a New Wave 213 nm ultraviolet laser system. An 80 µm spot size was used; with this system, this results in ~0.15 mJ/cm$^2$ on the sample. The laser is not tunable and is aging, such that this is full power at this spot size. Helium was used as a carrier gas and was set between 1.15 and 1.2 L/min. A Permian marine cement that was aragonite, now neomorphosed to calcite, was used as the standard (Walnut Canyon/Troy standard). This standard (which came from Rasbury and is fairly homogeneous, though far from perfect) is being

developed by the National Isotope Geosciences Laboratory at the British Survey and will be made available for others to use (Parrish et al., 2013). We did 30 s ablations in a sequence of five standards, five spots, two standards, five spots, etc., ending with five standards with 30 s between each spot for washout. The data were imported into Iolite (Paton et al., 2011), where baselines were subtracted, and downhole fractionation corrections were made based on the standard. The quality of the data was monitored by how closely the standard matched the U and Pb concentrations (4.5 and 0.17 ppm, respectively), ratios ($^{238}U/^{206}Pb = 22$, $^{207}Pb/^{206}Pb = 0.15$), and age (254 ±6 Ma). The $^{238}U/^{206}Pb$ ages calculated by Iolite were generally around 300 Ma, due to the common Pb in this sample. We did not make assumptions about the common Pb in our unknowns; the ages were calculated using the inverse concordia isochron in IsoExcel (Ludwig, 2012). The upper intercept is meaningless because of the common Pb, but the initial $^{207}Pb/^{206}Pb$ was used to monitor how good the data were, and the lower intercept provided an age for unaltered samples. We have applied this approach to carbonate samples that have been dated by our group by isotope dilution, and both ages match closely. The greater the spread in the data and the higher the concentrations, the lower are the uncertainties in the isochron and the more meaningful is the age.

Element maps were created by making ablation lines 100 µm apart. This leaves a small gap, so that the previous track does not interfere with the laser ablation, but through interpolation in Iolite, the maps are a good match to the rock fabric. The lines were compiled to make maps in Iolite based simply on counts. That is, although standards were run for comparison, they were not used to calculate concentrations of the elements. Relative differences in the maps distinguish phases (Fig. DR1 [see footnote 1]).

Four distinct generations or phases were recognized in this rock: the host rock, radiaxial cement, small veins, and the large white vein that appears to be the latest generation. Laser-ablation spots from these generations are shown in Figure DR1 (see footnote 1). By far the most favorable phase was the small veins with substantially higher U/Pb and lower $^{207}Pb/^{206}Pb$. The isochron age is based on only the data from the small veins, but the other data are plotted for comparison (Fig. DR2 [see footnote 1]). The concentrations and ratios are also found in Table DR1 (see footnote 1). The distinct nature of the U and Pb concentrations and ratios demonstrates that the small veins are distinct from the host rock.

Sixty-five spots were taken on the small vein in an attempt to maximize the range and lower the uncertainty on the age (two were left out because they were obviously partly in the host rock). We also tried to microsample this vein for isotope-dilution analyses (Fig. DR3 [see footnote 1]), but it was not possible to get enough material for a good analysis. The age of the small vein based on LA-ICP-MS is 77.1 ± 3.6 Ma (Fig. DR4 [see footnote 1]). Most of the data points overlap each other, so that a line is poorly defined. The few

data points that trend to lower U/Pb anchor the line. Based on comparison to the host rock, it is likely that there may be a host rock influence here.

The small veins are much more enriched in U and must have been for a long time to support their radiogenic (low $^{207}Pb/^{206}Pb$) values. Because the U/Pb is pretty high and the Pb is radiogenic, ages were calculated for each point based on a correction that made the standard give the right age (Fig. DR4 [see footnote 1]).

Carbonate Clumped Isotope Methodology and Modeling of Clumped Isotope Reordering

As described in the main text, we measured a series of samples, standards (the Cararra Marble), and heated gases over two analytical sessions. These data are presented in full in Table DR2 (see footnote 1). All data were processed using the $^{17}O/^{16}O$ ratio for Vienna standard mean ocean water (VSMOW) assumed by the Santrock correction scheme (Santrock et al., 1985). This value is suspected of being in error, but by an amount that does not lead to significant changes in $\delta^{13}C$ or $\Delta_{47}$ values for the compositions of samples examined in this study. Indeed, Schauer et al. (2016)demonstrated that when the difference between the $\delta^{13}C$ of the reference gas and sample is less than 10‰, as is the case for all samples in this study, the difference between the Santrock et al. (1985) and the more recent Brand et al. (2010) correction scheme is negligible. Equilibrated gases (25 °C) were analyzed as part of this study but were not sufficiently numerous and reproducible to provide a useful anchor for the “primary absolute reference frame” of Dennis et al. (2011). For this reason, we processed our carbonate sample measurements using the heritage “California Institute of Technology (CIT)” reference frame (Ghosh et al., 2006). All unknown samples analyzed in this study have $\Delta_{47}$ values within the range of those for the 21 carbonate standard analyses made in this study, and those standards yielded expected average values and experimental reproducibility similar to shot-noise mass spectrometric errors. For this reason, we are confident that no interpretations presented in this study were significantly biased by the reference frame used for data processing. We provide $\Delta_{47}$ values of carbonate samples recalculated for the “secondary absolute reference frame” based on heated gases and carbonate standards (Dennis et al., 2011). These latter values may have systematic uncertainties on the order of 0.01–0.02 ‰ and are given only as approximate guidelines to the values that would be expected for an independent study of these samples in a different laboratory.

The projection of samples into the absolute reference frame corrects the measured raw $\Delta_{47}$ value for nonlinearity of the mass spectrometer to yield a “true” $\Delta_{47}$ value. To do this, we used a slope for the heated gas line of 0.0065 for the Caltech mass spectrometer, as provided in Table 1 of Dennis et al. (2011). We then applied the empirical transfer function (ETF) to project the $\Delta_{47}$ value into the absolute reference frame. To do this, we again applied the

ETF slope of 1.1548 and ETF intercept of 0.9343 as provided in Table 1 of Dennis et al. (2011). Finally, we applied a correction factor to account for the isotopic fractionation between calcium carbonate and $CO_2$ for phosphoric acid as described in the methods section. This final number represents the approximate $\Delta_{47}$ in the absolute reference frame. Given the approximate nature of these values, we did not convert them to temperature using the calibration of Bonifacie et al. (2017).

Clumped isotope compositions and the associated temperatures presented in Tables 1 and 2 exceed those expected based on the known growth environments of the radiaxial and early equant cements analyzed as part of this study. For reasons described in the main text, we believe these clumped isotope temperatures have been impacted by thermally driven solid-state diffusion as a result of burial to temperatures significantly greater than their precipitation temperatures. We applied the model of Stolper and Eiler (2015) to back-calculate original precipitation temperatures. The details of this model can be found in the study of Stolper and Eiler (2015). Questions related to the model can be made directly to Prof. Stolper at the contact information provided in the original publication.

ACKNOWLEDGMENTS

We would like to thank ExxonMobil for permission to publish this manuscript. We also thank Kristin Bergmann and two anonymous reviewers for constructive suggestions that helped to improve this manuscript.

[1]GSA Data Repository item 2017343, elemental maps and complete analytical results from U-Pb and clumped isotope analysis of carbonate phases, is available at http://www.geosociety.org/datarepository/2017 or by request to editing@geosociety.org.

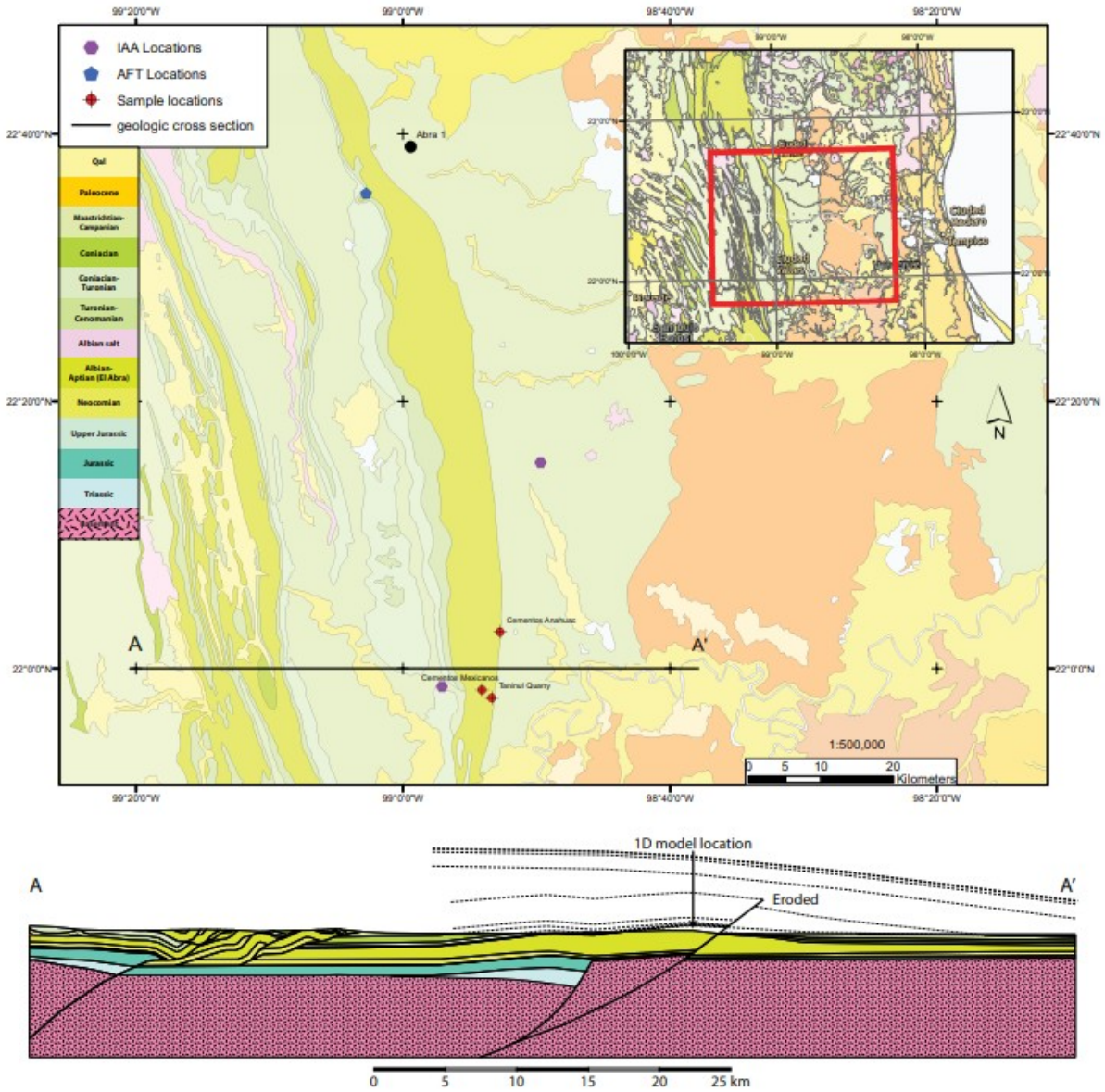


**Figure 1. Map of the study area, located in northeastern Mexico on the edge of the Valles–San Luis Potosi platform, exposed in Sierra de El Abra, near Cuidad Valles. The geologic map is based on Aguillón et al. (1999), and the location of the El Abra-1 well and sample locations for illite age analysis (IAA), apatite fission-track (AFT) analysis, U-Pb analysis, and the clumped isotope analysis discussed here are taken from Gray et al. (2001). The cross section was constructed solely on the basis of the published geologic map and should be considered schematic. However, the geologic map and cross section imply a Late Cretaceous basement-detached thrust system (the Sierra Madre Oriental) that was subsequently deformed by Paleogene basement-involved contractional deformation. Qal—Quaternary.**

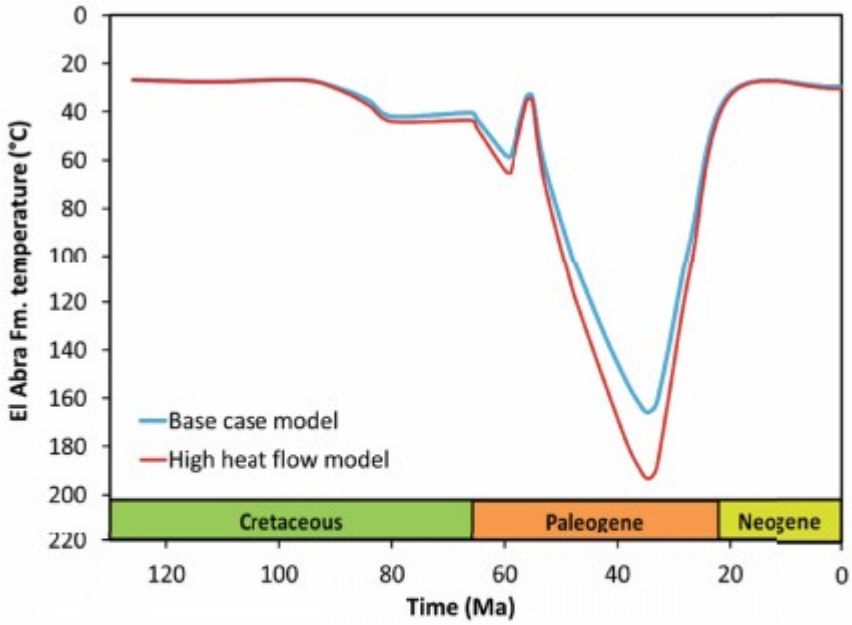


**Figure 2. Thermal history of the El Abra Formation at a central point between the sample locations in the Sierra de El Abra presented in Figure 1. Two thermal histories are provided: (1) a base case model (blue) that honors all constraints from illite age analysis (IAA), apatite fission-track (AFT), and fluid inclusion microthermometry, and (2) a high-heat-flow model (red) to test the sensitivity of clumped isotope reordering to the thermal history of the El Abra Formation.**

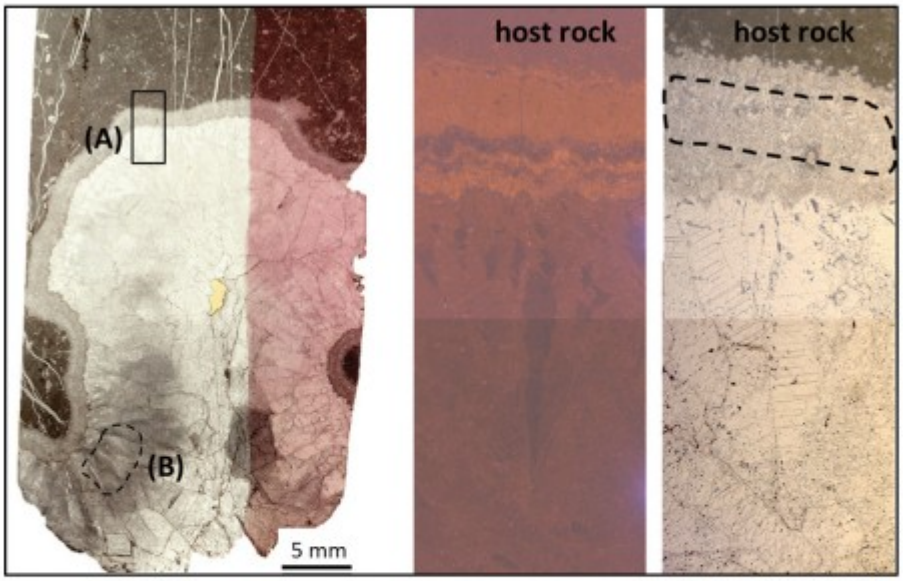


**Figure 3. Thin-section scan (left panel), cathodoluminescence (CL; center panel), and photomicrograph (right panel) images of sample CMEX 6. Approximate sampled area is outlined within the dashed line. Zone A was sampled for the fibrous, lining radiaxial calcite cement (R1), with the black box representing the region of the thin section imaged in the CL and photomicrograph images to the right. Zone B was sampled for the coarse radiaxial cement (R2). The CL image exhibits no obvious zoning, which suggests minimal recrystallization or alteration of this cement phase.**

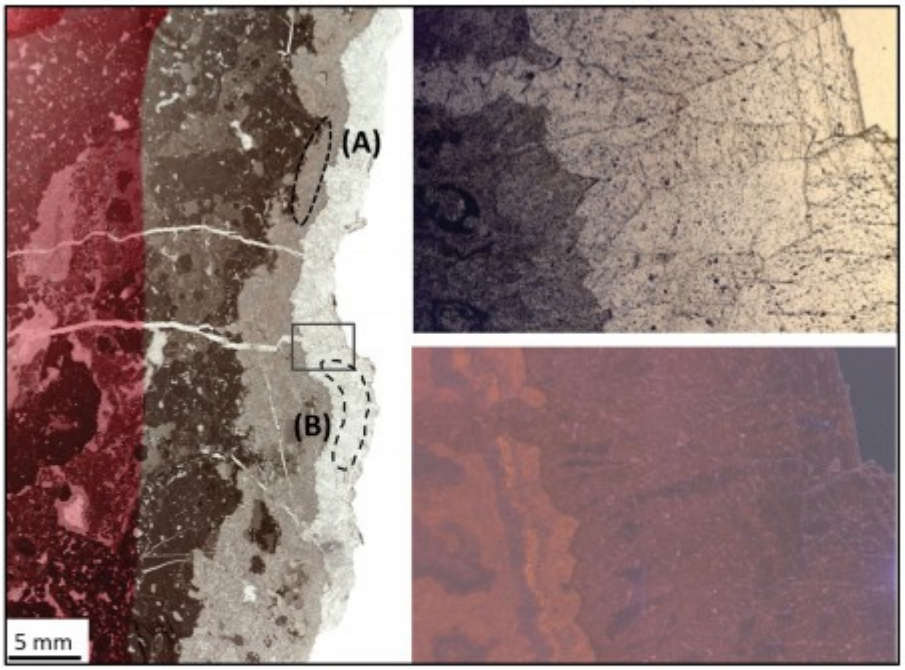


**Figure 4. Thin-section scan (left panel), cathodoluminescence (CL; lower-right panel) and photomicrograph (upper-right panel) images of sample CMEX 3. Approximate sampled area is outlined within the dashed line. Zone A was sampled for the fibrous, lining radiaxial calcite cement (R1). Zone B was sampled for the coarse, equant cement, with the black box representing the region of the thin section imaged in the CL and photomicrograph images to the right. The CL image exhibits no obvious zoning, which suggests minimal recrystallization or alteration of this cement phase.**

TABLE 1. CARBON AND OXYGEN ISOTOPE SIGNATURES OF THE CEMENT PHASES SAMPLED IN THIS STUDY

| Sample ID | Paragenetic phase | *n* | Timing order | $\delta^{13}C$ (‰, VPDB) | $\delta^{18}O$ (‰, VPDB) | $\Delta_{47}$ (‰) | $\Delta_{47}$ ARF (‰) |
|---|---|---|---|---|---|---|---|
| CAN-9A | Matrix | 2 | | 2.08 ± 0.02 | −5.08 ± 0.08 | 0.488 ± 0.006 | 0.547 |
| CMEX3 | Lining radiaxial cement (R1) | 1 | 1 | 2.47 | −2.46 | 0.528 ± 0.011 | 0.633 |
| CMEX6 | Lining radiaxial cement (R1) | 1 | 1 | 2.54 | −1.96 | 0.527 ± 0.020 | 0.632 |
| CMEX6 | Coarse radiaxial cement (R2) | 2 | 2 | 1.55 ± 0.01 | −5.22 ± 0.01 | 0.492 ± 0.004 | 0.591 |
| CMEX3 | Equant cement (E1) | 2 | 3 | 1.67 ± 0.04 | −5.17 ± 0.04 | 0.462 ± 0.002 | 0.517 |
| TAN104 | Equant cement (E1) | 2 | 3 | 0.84 ± 0.01 | −7.91 ± 0.28 | 0.413 ± 0.002 | 0.452 |
| TAN101 | Vug-fill cement (E2) | 1 | 4 | 0.37 | −11.81 | 0.506 ± 0.015 | 0.586 |
| CAN11A | Vug-fill cement (E2) | 2 | 4 | 0.90 ± 0.02 | −12.93 ± 0.03 | 0.518 ± 0.003 | 0.560 |

*Note*: Relative timing is given for each paragenetic phase studied. Carbonate clumped isotope signature is reported in the Caltech reference frame (Ghosh et al., 2006) and the absolute reference frame ($\Delta_{47}$ ARF; Dennis et al., 2011). Analytical uncertainty is reported as ±1σ based on replicate analysis of individual samples. VPDB—Vienna Peedee belemnite.

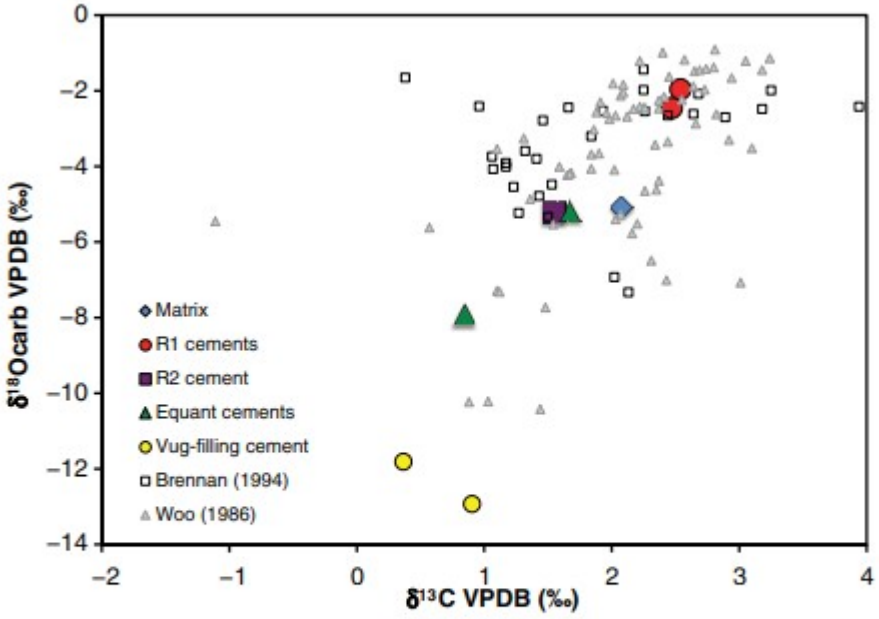


**Figure 5. Oxygen and carbon isotope compositions (Vienna Peedee belemnite [VPDB] scale) of the different generations of calcite cement phases from the El Abra Formation. Uncertainties (1σ) for $\delta^{18}O$ and $\delta^{13}C$ are 0.057‰ and 0.028‰, respectively, based on reproducibility of the Carrara marble standard. Error bars are smaller than the symbol size. Data from the studies of Woo (1986) and Brennan (1994) is provided for reference.**

TABLE 2. TEMPERATURES OF THE DIFFERENT CEMENT GENERATIONS AND $\Delta^{18}O_{VSMOW}$ VALUES OF THE PARENT FLUID FROM WHICH THEY PRECIPITATED

| Sample ID | Paragenetic phase | Raw temp (°C) | ±1σ | Raw $\delta^{18}O_{VSMOW}$ (‰) | ±1σ |
|---|---|---|---|---|---|
| CAN-9A | Matrix | 83 | 10 | 7.2 | 1.5 |
| CMEX3 | Lining radiaxial cement (R1) | 64 | 8 | 6.9 | 1.3 |
| CMEX6 | Lining radiaxial cement (R1) | 64 | 9 | 7.5 | 1.4 |
| CMEX6 | Coarse radiaxial cement (R2) | 81 | 10 | 6.8 | 1.5 |
| CMEX-3 | Equant cement (E1) | 97 | 11 | 9.1 | 1.5 |
| TAN104 | Equant cement (E1) | 134 | 17 | 10.8 | 1.9 |
| TAN101 | Vug-fill cement (E2) | 74 | 9 | −0.9 | 1.4 |
| CAN-11A | Vug-fill cement (E2) | 68 | 9 | −3.0 | 1.4 |

*Note*: Temperatures were calculated from the measured values and are reported to the nearest °C (Ghosh et al., 2006). $\delta^{18}O_{VSMOW}$ (VSMOW—Vienna standard mean ocean water) was calculated from the raw measured carbonate clumped isotope temperatures (Kim and O'Neil, 1997). Uncertainty in raw temperature and $\delta^{18}O$ is based on the larger of either standard or sample reproducibility of the sample average temperature. We did not consider uncertainty in the clumped isotope temperature calibration in this uncertainty estimate.

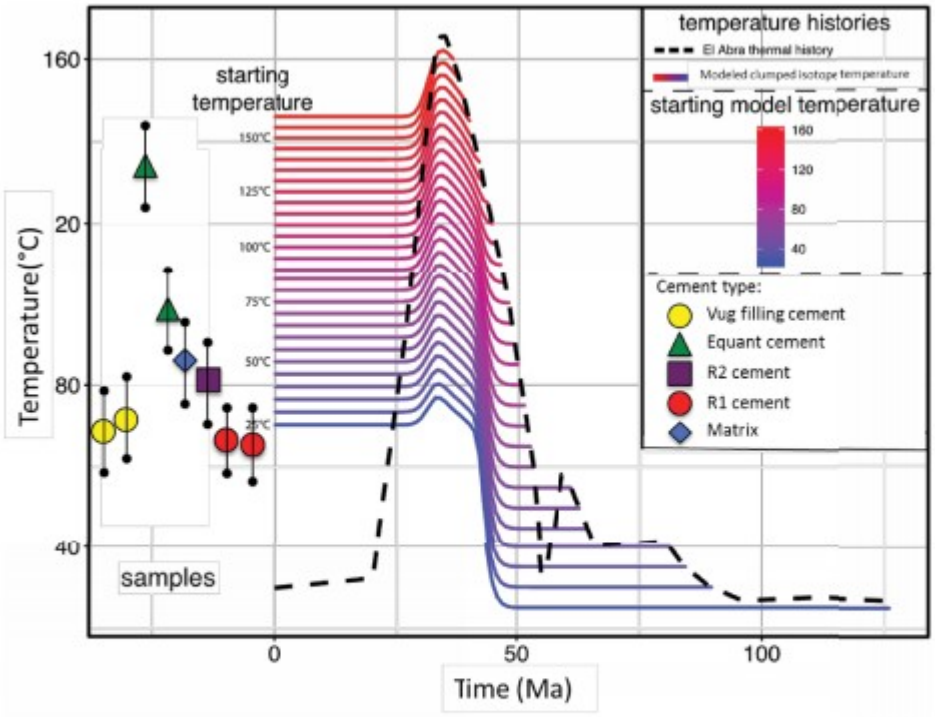


**Figure 6. Evolution in $\Delta_{47}$ clumped isotope temperatures of the calcite cements analyzed in this study for the base case time-temperature history of the El Abra Formation. Measured $\Delta_{47}$ clumped isotope temperatures are provided at time = 0, with corrected values derived through reverse application of the paired "reaction-diffusion" reordering model of Stolper and Eiler (2015). Error bars represent the uncertainty associated with the measured $\Delta_{47}$ temperatures.**

TABLE 3. RESTORED TEMPERATURES CALCULATED USING THE KINETIC MODEL OF STOLPER AND EILER (2015)

| Sample ID | Minimum temperature (°C) | Restored temperature (°C) | Maximum temperature (°C) | Minimum age (Ma) | Restored age (Ma) | Maximum age (Ma) | Restored $\delta^{18}O_{VSMOW}$ (‰) |
|---|---|---|---|---|---|---|---|
| CAN-9A | 31 | 46 | 64 | 52 | 65 | 89 | 1.3 ± 2.8 |
| CMEX3 | 2 | 15 | 29 | 89 | 125 | 125 | –2.2 ± 3.1 |
| CMEX6 | 2 | 15 | 30 | 89 | 125 | 125 | –1.6 ± 3.1 |
| CMEX6 | 28 | 43 | 60 | 53 | 80 | 93 | 0.54 ± 2.8 |
| CMEX-3 | 52 | 70 | 92 | 54 | 52 | 50 | 5.2 ± 2.7 |
| TAN104 | 108 | 138 | 149 | 33 | 42 | 46 | 11.1 ± 2.8 |
| TAN101 | N/A | N/A | N/A | 25 | 25 | 25 | –0.9 |
| CAN-11A | N/A | N/A | N/A | 25 | 25 | 25 | –3.0 |

*Note*: Minimum and maximum restored temperatures were calculated by propagating through the uncertainty in the measured temperature in the model. Cement ages were determined by integrating the restored temperatures and associated uncertainties with the thermal history. Restored and $\delta^{18}O_{VSMOW}$ (VSMOW—Vienna standard mean ocean water) values were calculated for the range in temperatures using the equation from Kim and O'Neil (1997). N/A denotes not applicable because these phases precipitated during exhumation and so did not experience elevated temperatures.

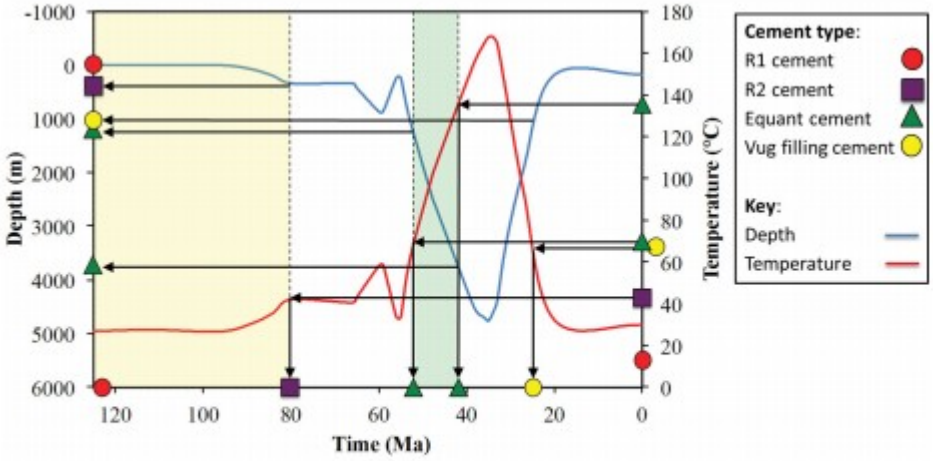


**Figure 7. Depth below mud line vs. time vs. temperature of the El Abra Formation. The restored temperatures for the four generations of cements are plotted to determine the timing and depth of precipitation for each of the cements.**

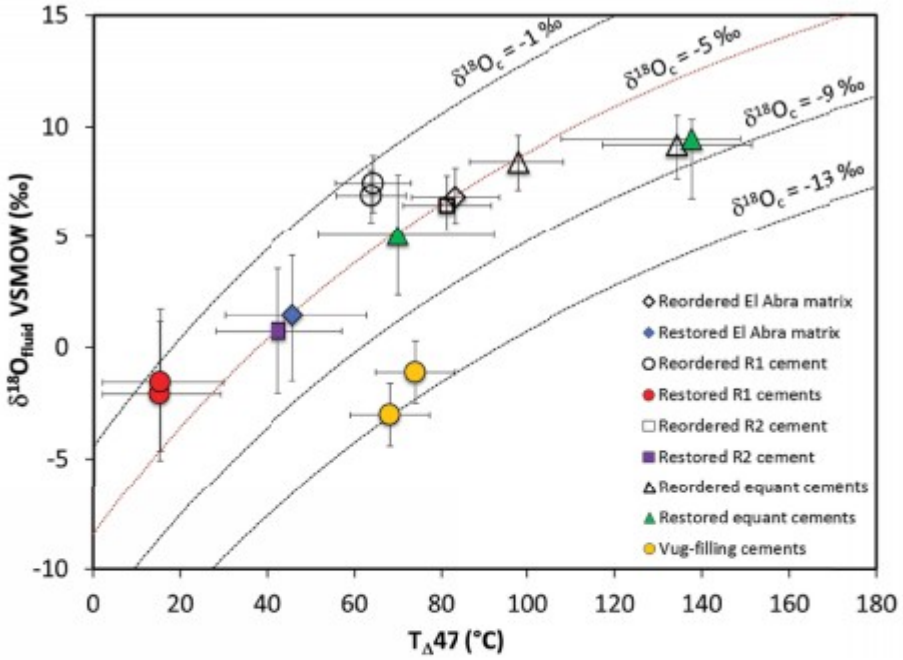


**Figure 8.** $\delta^{18}O_{VSMOW}$ of the parent fluid vs. $\Delta_{47}$ clumped isotope temperature for the different generations of cements of the El Abra Formation. The $\delta^{18}O_{VSMOW}$ values were calculated using both measured and restored clumped isotope formation temperatures (along with $\delta^{18}O_{VDPB}$ values of carbonate). Gray dashed lines represent the evolution in $\delta^{18}O_{VSMOW}$ as a function of temperature for constant $\delta^{18}O_{VPDB}$ values of carbonate (Kim and O'Neil, 1997). Temperature uncertainties are based on 1 standard deviation of the reproducibility of standards analyzed in the study. Analytical uncertainties were propagated through the model to derive the uncertainty in the restored temperatures. The $\delta^{18}O$ uncertainties were also calculated for uncorrected temperatures by propagating the uncertainty in the measured clumped isotope temperature. VSMOW—Vienna standard mean ocean water.

References

Aguillón, G.F., García, R.C., De León, A.G.D., Macías, P.R.M., Aguilera, J.M.T., Villaseñor, F.J.O., Mendoz, O.R., Amaral, C.C., Valdez, G.A., and Tanguma, M.M., 1999, Cartas Geológico-Mineras y Geoquimicas, Cuidad Mante F14-5: Pachuca, Servicio Geólogico Mexicano, scale 1:250,000.

Allan, J.R., and Matthews, R.K., 1982, Isotope signatures associated with early meteoric diagenesis: Sedimentology, v. 29, p. 797–817, http://doi.org/10.1111/ j.1365-3091.1982.tb00085.x.

Bonifacie, M., Calmels, D., Eiler, J.M., Horita, J., Chaduteau, C., Vasconcelos, C., Agrinier, P., Katz, A., Passey, B.H., Ferry, J.M., and Bourrand, J.J., 2017, Experimental calibration of the dolomite clumped isotope thermometer from 25 to 350°C, and implications for a universal calibration for all (Ca, Mg, Fe)CO3 carbonates: Geochimica et Cosmochimica Acta, v. 200, p. 255–279, http://doi.org/10.1016/j.gca.2016.11.028.

Brand, W.A., Assonov, S.S., and Coplen, T.B., 2010, Correction for the 17O interference in δ( 13C) measurements when analyzing CO2 with stable isotope mass spectrometry (IUPAC Technical Report): Pure and Applied Chemistry, v. 82, p. 1719–1733, http://doi.org/10.1351/PAC-REP-09-01-05.

Brennan, S.T., 1994, Impact of Fluid and Thermal History on Reservoir Properties of El Abra Limestone, Sierra el Abra, Mexico [M.S. thesis]: Lawrence, Kansas, University of Kansas, 183 p.

Bristow, T.F., Bonifacie, M., Derkowski, A., Eiler, J.M., and Grotzinger, J.P., 2011, A hydrothermal origin of isotopically anomalous cap dolostone cements from south China: Nature, v. 474, p. 68–71, http://doi.org/10.1038/nature10096.

Budd, D.A., Frost, E.L., Huntington, K.W., and Allwardt, P.F., 2013, Syndepositional deformation features in high-relief carbonate platforms: Long-lived conduits for diagenetic fluids: Journal of Sedimentary Research, v. 83, p. 12–36, http://doi.org/10.2110/jsr.2013.3.

Choquette, P.W., and Pray, L.C., 1970, Geologic nomenclature and classification of porosity in sedimentary carbonates: American Association of Petroleum Geologists Bulletin, v. 54, p. 207–250.

Dale, A., John, C.M., Mozley, P.S., Smalley, P.C., and Muggeridge, A.H., 2014, Time-capsule concretions: Unlocking burial diagenetic processes in the Mancos Shale using carbonate clumped isotopes: Earth and Planetary Science Letters, v. 394, p. 30–37, http://doi .org/10.1016/j.epsl.2014.03.004.

Dennis, K.J., and Schrag, D.P., 2010, Clumped isotope thermometry of carbonatites as an indicator of diagenetic alteration: Geochimica et Cosmochimica Acta, v. 74, p. 4110–4122, http://doi.org/10.1016/j .gca.2010.04.005.

Dennis, K.J., Affek, H.P., Passey, B.H., Schrag, D.P., and Eiler, J.M., 2011, Defining an absolute reference frame for ‘clumped isotope’ studies of CO2 : Geochimica et Cosmochimica Acta, v. 75, p. 7117–7131, http://doi .org/10.1016/j.gca.2011.09.025.

Eiler,J.M., 2007, “Clumped-isotope” geochemistry—The study of naturally-occurring, multiply-substituted isotopologues: Earth and Planetary Science Letters, v. 262, p. 309–327, http://doi.org/10.1016/j.epsl.2007.08.020.

Epstein, S., Buchsbaum, R., Lowenstam, H.A., and Urey, H.C., 1953, Revised carbonate-water isotopic temperature scale: Geological Society of America Bulletin, v. 64, p. 1315–1326, http://doi.org/10.1130/0016 -7606(1953)64[1315:RCITS]2.0.CO;2.

Ferry, J.M., Passey, B.H., Vasconcelos, C., and Eiler, J.M., 2011, Formation of dolomite at 40–80 °C in the Latemar carbonate buildup, Dolomites, Italy, from clumped isotope thermometry: Geology, v. 39, p. 571– 574, http://doi.org/10.1130/G31845.1.

Frakes, L.A., Francis, J.E., and Syktus, J.I., 1992, Climate Modes of the Phanerozoic: Cambridge, UK, Cambridge University Press, 274 p., http://doi.org/10.1017/ CBO9780511628948.

Galloway, W.E., Ganey-Curry, P.E., Li, X., and Buffler, R.T., 2000, Cenozoic depositional history of the Gulf of Mexico basin: American Association of Petroleum Geologists Bulletin, v. 84, p. 1743–1774.

Ghosh, P., Adkins, J., Affek, H., Balta, B., Guo, W., Schauble, E.A., Schrag, D., and Eiler, J.M., 2006, 13C-18O bonds in carbonate minerals: A new kind of paleothermometer: Geochimica et Cosmochimica Acta, v. 70, p. 1439–1456, http://doi.org/10.1016/j .gca.2005.11.014.

Gray, G.G., and Lawton, T.F., 2011, New constraints on timing of Hidalgoan (Laramide) deformation in the Parras and La Popa basins, NE Mexico: Boletín de la Sociedad Geológica Mexicana, v. 63, p. 333–343.

Gray, G.G., Pottorf, R.J., Yurewicz, D.A., Mahon, K.I., Pevear, D.R., and Chuchla, R.J., 2001, Thermal and chronological record of syn- to post-Laramide burial and exhumation, Sierra Madre Oriental, Mexico, in Bartolini, C., Buffler, R.T., and Cantu-Chapa, A., eds., The Western Gulf of Mexico Basin: Tectonics, Sedimentary Basins, and Petroleum Systems: American Association of Petroleum Geologists Memoir 75, p. 159–181.

Guzman, E.J., and De Cserna, Z., 1963, Tectonic history of Mexico, in Childs, O.E., and Beebe, B.W., eds., Backbone of the Americas—Tectonic History from Pole to Pole: American Association of Petroleum Geologists Memoir 2, p. 113–129.

Henkes, G.A., Passey, B.H., Grossman, E.L., Shenton, B.J., Perez-Huerta, A., and Yancey, T.E., 2014, Temperature limits for preservation of primary calcite clumped isotope paleotemperatures: Geochimica et Cosmochimica Acta, v. 139, p. 362–382, http://doi.org/10.1016/j .gca.2014.04.040.

Huang, W.-L., Longo, J.M., and Pevear, D.R., 1993, An experimentally derived kinetic model for smectiteto-illite conversion and its use as a geothermometer: Clays and Clay Minerals, v. 41, p. 162–177, http://doi .org/10.1346/CCMN.1993.0410205.

Huntington, K.W., Eiler, J.M., Affek, H.P., Guo, W., Bonifacie, M., Yeung, L.Y., Thiagarajan, N., Passey, B., Tripati, A., Daëron, M., and Came, R., 2009, Methods and limitations of ‘clumped’ CO2 isotope (Δ47) analysis by gas-source isotope ratio mass spectrometry: Journal of Mass Spectrometry, v. 44, p. 1318–1329, http://doi .org/10.1002/jms.1614.

Huntington, K.W., Budd, D.A., Wernicke, B.P., and Eiler, J.M., 2011, Use of clumped-isotope thermometry to constrain the crystallization temperature of diagenetic calcite: Journal of Sedimentary Research, v. 81, p. 656–669, http:// doi.org/10.2110/jsr.2011.51.

Ketcham, R.A., 2005, Forward and inverse modeling of low-temperature thermochronometric data: Reviews in Mineralogy and Geochemistry, v. 58, p. 275–314, http://doi.org/10.2138/rmg.2005.58.11.

Ketcham, R.A., Carter, A., Donelick, R.A., Barbarand, J., and Hurford, A.J., 2007, Improved modeling of fission-track annealing in apatite: The American Mineralogist, v. 92, p. 799–810, http://doi.org/10.2138/ am.2007.2281.

Kim, S.T., and O'Neil, J.R., 1997, Equilibrium and nonequilibrium oxygen isotope effects in synthetic carbonates: Geochimica et Cosmochimica Acta, v. 61, p. 3461– 3475, http://doi.org/10.1016/S0016-7037(97)00169-5.

Kim, Y., and Lee, Y.I., 2003, Radiaxial fibrous calcites as low-magnesian calcite cement precipitated in a marine-meteoric mixing zone: Sedimentology, v. 50, p. 731–742, http://doi.org/10.1046/j.1365-3091.2003 .00573.x.

Lloyd, M.K., Eiler, J.M., and Nabelek, P.I., 2017, Clumped isotope thermometry of calcite and dolomite in a contact metamorphic environment: Geochimica et Cosmochimica Acta, v. 197, p. 323–344, http://doi .org/10.1016/j.gca.2016.10.037.

Ludwig, K. R., 2012, User's Manual for Isoplot 3.75, A Geochronological Toolkit for Microsoft Excel: Berkeley Geochronology Center Special Publication 5, 75 p.

McCrea, J.M., 1950, On the isotopic chemistry of carbonates and a paleotemperature scale: The Journal of Chemical Physics, v. 18, p. 849–857, http://doi.org/10. 1063/1.1747785.

Minero, C.J., 1988, Sedimentation and diagenesis along an island-sheltered platform margin, El Abra Formation, Cretaceous of Mexico, in James, N.P., and Choquette, P.W., eds., Paleokarst: Berlin, Springer-Verlag, p. 385– 405, http://doi.org/10.1007/978-1-4612-3748-8_19.

Minero, C.J., 1991, Sedimentation and diagenesis along open and island-protected windward carbonate platform margins of the Cretaceous El Abra Formation, Mexico: Sedimentary Geology, v. 71, p. 261–288, http://doi.org/10.1016/0037-0738(91)90106-N.

Parrish, R.R., Horstwood, M., Austin-Giddings, W., Roberts, N., Condon, D., and Rasbury, T., 2013, In situ U-Pb dating of carbonate by LA-ICP-(MC)-MS and IDTIMS: Mineralogical Magazine, v. 77, p. 1927.

Passey, B.H., and Henkes, G.A., 2012, Carbonate clumped isotope bond reordering and geospeedometry: Earth and Planetary Science Letters, v. 351, p. 223–236, http://doi.org/10.1016/j.epsl.2012.07.021.

Passey, B.H., Levin, N., Cerling, T.E., Brown, F.H., and Eiler, J.M., 2010, High-temperature environments of human evolution in East Africa based on bond ordering in paleosol carbonates: Proceedings of the National Academy of

Sciences of the United States of America, v. 107, p. 11,245–11,249, http://doi.org/10.1073/ pnas.1001824107.

Paton, C., Hellstrom, J., Paul, B., Woodhead, J., and Hergt, J., 2011, Iolite: Freeware for the visualisation and processing of mass spectrometric data: Journal of Analytical Atomic Spectrometry, v. 26, p. 2508–2518, http:// doi.org/10.1039/c1ja10172b.

Pevear, D.R., 1999, Illite and hydrocarbon exploration: Proceedings of the National Academy of Sciences of the United States of America, v. 96, p. 3440–3446, http:// doi.org/10.1073/pnas.96.7.3440.

Pottorf, R.J., Gray, G.G., Kozar, M.G., Fitchen, W.M., Richardson, M., Chuchla, R.J., and Yurewicz, D.A., 1996, Hydrocarbon generation and migration in the Tampico segment of the Sierra Madre Oriental fold-thrust belt: Evidence from an exhumed oil field in the Sierra de El Abra, in Gomez-Luna, M.E., and Martinez-Cortez, A., eds., Memorias del Congreso Latinoamericano de Geoquimica Organics, Cancun, Mexico, p. 100–101.

Ritter, A.C., Kluge, T., Berngt, J., Richter, D.K., John, C.M., Bodin, S., and Immenhauser, A., 2015, Application of redox sensitive proxies and carbonate clumped isotopes to Mesozoic and Palaeozoic radiaxial fibrous calcite cements: Chemical Geology, v. 417, p. 306–321, http://doi.org/10.1016/j.chemgeo.2015.10.008.

Santrock, J., Studley, S.A., and Hayes, J.M., 1985, Isotopic analyses based on the mass spectra of carbon dioxide: Analytical Chemistry, v. 57, p. 1444–1448, http://doi .org/10.1021/ac00284a060.

Schauble, E.A., Ghosh, P., and Eiler, J.M., 2006, Preferential formation of 13C-18O bonds in carbonate minerals, estimated using first-principles lattice dynamics: Geochimica et Cosmochimica Acta, v. 70, p. 2510– 2529, http://doi.org/10.1016/j.gca.2006.02.011.

Schauer, A.J., Kelson, J., Saenger, C., and Huntington, K.W., 2016, Choice of 17O correction affects clumped isotope (Δ47) values of CO2 measured with mass spectrometry: Rapid Communications in Mass Spectrometry, v. 30, p. 2607–2616, http://doi.org/10.1002/rcm.7743.

Shackleton, N., and Kennett, J., 1975, Paleotemperature history of the Cenozoic and the initiation of Antarctic glaciation: Oxygen and carbon isotope analyses in DSDP Sites 277, 279 and 281, in Kennett, J.P., Houtz, R.E., Andrews, P. B., Edwards, A.R., Gostin, V.A., Hajós, M., Hampton, M.A., Jenkins, D.G., Margolis, S.V., Ovenshine, A.T., PerchNielsen, K., White, S.M., eds., Initial Reports of the Deep Sea Drilling Project, Volume 29: Washington, D.C., U.S. Government Printing Office, p. 743–755.

Shenton, B.J., Grossman, E.L., Passey, B.H., Henkes, G.A., Becker, T.P., Laya, J.C., Perez-Huerta, A., Becker, S.P., and Lawson, M., 2015, Clumped isotope thermometry in deeply buried sedimentary carbonates: The effects of bond

reordering and recrystallization: Geological Society of America Bulletin, v. 127, p. 1036–1051.

Stolper, D.A., and Eiler, J.M., 2015, The kinetics of solidstate isotope-exchange reactions for clumped isotopes: A study of inorganic calcites and apatites from natural and experimental samples: American Journal of Science, v. 315, p. 363–411, http://doi.org/10.2475/ 05.2015.01.

Suter, M., 1984, Cordilleran deformation along the eastern edge of the Valles–San Luis Potosi carbonate platform, Sierra Madre Oriental fold-thrust belt, east-central Mexico: Geological Society of America Bulletin, v. 95, p. 1387–1397, http://doi.org/10.1130/0016-7606(1984)952.0.CO;2.

Swart, P.K., Burns, S.J., and Leder, J.J., 1991, Fractionation of the stable isotopes of oxygen and carbon in carbon dioxide during the reaction of calcite with phosphoric acid as a function of temperature and technique: Chemical Geology, v. 86, p. 89–96.

Winkelstern, I.Z., and Lohmann, K.C., 2016, Shallow burial alteration of dolomite and limestone clumped isotope geochemistry: Geology, v. 44, p. 467–470, http://doi .org/10.1130/G37809.1.

Wolfe, Z.D., 2012, Stratigraphic Controls on the Structural Evolution of the Sierra Madre Oriental Fold-Thrust Belt, Eastern Mexico [M.S. thesis]: Houston, Texas, University of Houston, 58 p.

Woo, K.S., 1986, Textural-Isotopic-Chemical Studies of Mid-Cretaceous Limestones: Implications for Carbonate Diagenesis and Paleoceanography [Ph.D. dissertation]: Urbana-Champaign, Illinois, University of Illinois at Urbana-Champaign, 246 p.

Woo, K.S., Anderson, T.F., and Sandberg, P.A., 1993, Diagenesis of skeletal and nonskeletal components of Mid-Cretaceous limestones: Journal of Sedimentary Petrology, v. 63, p. 18–32.

Wygrala, B.P., 1989, Integrated Study of an Oil Field in the Southern Po Basin, Northern Italy [Ph.D. dissertation]: Cologne, Germany, University of Cologne, 217 p.

Yarbuh, I., and Contreras, J., 2017, The interplay between deformation, erosion and sedimentation in the deepwater Mexican Ridges foldbelt, western Gulf of Mexico basin: Basin Research, v. 29, p. 446–464, http://doi .org/10.1111/bre.12157.

Zhou, J., Poulsen, C.J., Pollard, D., and White, T.S., 2008, Simulation of modern and middle Cretaceous marine δ18O with an ocean-atmosphere general circulation model: Paleoceanography, v. 23, PA3223, http://doi.org/ 10.1029/2008PA001596.